Jurnal Tribologi 49 (2026) 249-272

MYTRIBOS Malaysian Tribology Society

Jurnal Tribologi

Website : jurnaltribologi.mytribos.org e-issn: 2289-7232

The impact of bearing profile variation on the tribological performance of journal bearing under shaft misalignment

Moneer H. Tolephih [1], Hazim U. Jamali [2], Helen A. Almosawy [2], Oday Abdullah [3,4*], Zahraa A. AL-Dujaili [2]

[1] Al-Naji University, Al Yarmouk, 10015 Baghdad, IRAQ.
[2] University of Kerbala, Kerbala, 56001 Kerbala, IRAQ.
[3] University of Baghdad, Aljadria street, 47024 Baghdad, IRAQ.
[4] Al-Farabi Kazakh National University, Almaty, 050040 Almaty, KAZAKHSTAN.
*Corresponding author: oday.abdullah@coeng.uobaghdad.edu.iq

KEYWORDS

Journal bearing
Finite length
Stability
Deviation
Modification

ABSTRACT

The performance characteristics of journal bearings are strongly related to the shaft misalignment. This deviation results occurred due to many reasons such as deformation of the shaft, manufacture errors, installation errors, bearing wear, etc. Misalignment causes a sharp drop in lubricant film thickness and a significant increase in the levels of pressure, which may result in direct contact between the journal and the bearing inner surface under severe levels of misalignment. The negative consequences of such cases can be reduced by using a sufficient profile design of the bearing. This paper investigates the effect of modifying finite-length journal bearings design using linear and curved profiles to predict the pressure distribution, film thickness, and system stability. A numerical solution of the governing equations is performed based on the finite difference method considering the 3D shaft misalignment effect. The presence of misalignment increases the pressure level by 53 % and decreases the minimum film thickness by 80% which has a negative impact on the performance of the system. The results illustrated that the curved modification of the profile resulted in positive consequences on bearing performance. This includes a reduction of 21% in the maximum pressure level and an increase of 26.4% in the journal critical speed. Furthermore, the film thickness level is elevated significantly due to this modification despite the extreme misalignment levels.

Received 14 February 2025; received in revised form 4 May 2025; accepted 16 May 2025.
To cite this article: Tolephih et al. (2026). The impact of bearing profile variation on the tribological performance of journal bearing under shaft misalignment. Jurnal Tribologi 49, pp.249-272.

1.0 INTRODUCTION

The performance of rotating types of machinery relies significantly on the performance of the journal-bearing system. The need for high levels of power output in modern applications increases the machinery speed which raises the stability problems of rotors that depend on such types of bearings. In general, stability has significant considerations in high-speed applications. It is well known that the stability of the system depends on journal bearing geometry, rotor speed, loading conditions, and lubricant properties. Therefore, the related factors that are used in determining the stability of journal bearings are critical speed, whirl frequency ratio, and equivalent stiffness. The higher critical speed leads to more stability of journal-bearing. The condition of perfectly aligned journal bearing may not exist in practical applications due to many reasons. Misalignment results due to deformation of the shaft, manufacture errors, installation errors, bearing wear, etc. Although misalignment increases critical speed (Rao, 2012), it also increases the maximum pressure levels accompanied by a significant drop in the minimum film thickness (Al-Dujaili et al., 2020). This means a reduction in the load-carrying capacity of the system based on a design threshold for the lubricant thickness. Consequently, the engineers should balance between the load-carrying capacity and the critical speed of the system. Axial profile modification (chamfer) is one of the solutions to reduce the maximum pressure and to improve the level of film thickness which is also commonly used on gear teeth and cam-follower mechanisms (Jamali et al., 2015; Miyanaga and Tomioka, 2019; Jamali et al., 2019; Al-Hamood et al., 2019; Jamali et al., 2013). The stability of misaligned journal bearings has been investigated by researchers because of the common use of such types of bearings in the industry. Qiu and Tieu, 1995 determined the static and dynamic characteristics in addition to the system stability threshold considering the effect of misalignment under different values of eccentricity ratio. Papadopoulos et al., 2008 also considered misalignment in the stability of a rigid rotor. Tieu and Qiu, 1995 performed a comparison between the results of linear theory and that from nonlinear simulation where the bearing forces were obtained from the pressure distribution using Reynolds boundary conditions. They illustrated that the critical speeds are the same for the two methods of solution. However, they mentioned that the shaft trajectories are slightly difference. They did not consider the misalignment effect and bearing modification. Strzelecki, 2005 considered bearing modification only over the total bearing length where the characteristics of the aligned and misaligned systems were calculated. However, the effect of profile modification on the stability of the journal bearing was not taken into consideration. Ogrodnik et al., 2011 investigated the effect of dimensional manufacturing tolerances on the stability of journal bearing without considering the misalignment effect. The experimental data showed that the error created by these manufacturing tolerances in estimating the oil film instability may reach ±20%. Nicoletti, 2013 improved the rotor margins of stability by optimizing the bearing profiles. Stability margins were predicted and the solutions were obtained in terms of the Somerfield number and the number of control points. The bearing profile was described by control points that define the clearance of the bearing at each angular position. The outcome of the work explained that the required profile of the bearing can be determined to enhance the stability limits for ideally aligned bearings. Xu et al., 2015 studied the effect of journal out of roundness on the performance of journal bearings where they explained how it affects the bearing dynamic coefficients. Mehrjardi et al., 2016 investigated the performance of non-circular finite length journal bearings with two and three lobes where they analyzed the journal bearing stability based on the linear and nonlinear solutions. Miraski et al., 2017 used a numerical solution to calculate the dynamic coefficients of bearings with finite length under laminar and turbulent regimes. Their results

showed that at a high Somerfield number and low load, the flow type did not affect the system stability. Yadav et al., 2019 studied the dynamic characteristics of two lobes journal bearing considering the non-Newtonian effect of the lubricant. The solution was based on the finite element method, and the mathematical model was solved considering the Runge-Kutta solution method to determine the system stability limit. Sun et al., 2019 investigated the errors related to the shape of the journal and their effects on the system's dynamic response. Jain and Sharma, 2017 analyzed the linear and nonlinear motion of two lobes of hybrid journal bearing based on a numerical simulation of the journal center rotation path. Shi et al., 2020 used numerical solutions to obtain the dynamic characteristics of the journal bearings. The effect of rotation speed and eccentricity ratio on the dynamic performance of the journal bearing were investigated in detail. Jamali and Al-Hamood, 2018 presented a general method to consider the effect of misalignment in the analyses of journal bearing problems. Chen et al., 2019 suggested a method to identify the dynamic characteristics of circular journal bearing through a combination between a proposed complemented equation and the dynamic equations which found from the unbalance response. Al-Dujaili et al., 2020 investigated the misalignment effects in journal bearings by modifying the bearing profile without studying the effect of this modification on the stability of journal bearings.

This work presents a numerical solution for finite-length journal bearings to predict the critical speed of the system and to reduce the misalignment effect on the bearing performance. The modification of the axial bearing profile (chamfer) is considered in the analysis, which is used to avoid the thinning in the lubricant thickness under misalignment. Two forms of this modification are used in this work, and the solution involves a general 3D misalignment model. The misalignment model considers the shift in the journal in the horizontal and vertical directions. The pressure and film thickness levels are evaluated under different levels of misalignment and chamfer.

2.0 GOVERNING EQUATIONS

The main governing equation in this problem is the Reynolds equation which is given by (Chasalevris and Sfyris, 2013):

$$\frac{\partial}{\partial x}\left(h^3\frac{\partial p}{\partial x}\right)+\frac{\partial}{\partial z}\left(h^3\frac{\partial p}{\partial z}\right)=6\eta r\omega\ \frac{\partial h}{\partial x} \tag{1}$$

The equation of film thickness is (Jamali and Al-Hamood, 2018):

$$h=c(1+\varepsilon_r\ \cos(\theta)) \tag{2}$$

The dimensionless forms of these equations are:

$$\frac{\partial}{\partial \theta}\left(H^3\frac{\partial P}{\partial \theta}\right)+(\frac{R}{L})^2\frac{\partial}{\partial Z}\left(H^3\frac{\partial P}{\partial Z}\right)=\ \frac{\partial H}{\partial \theta} \tag{3}$$

$$H=1+\varepsilon_r\ \cos(\theta) \tag{4}$$

where,

$$P = \frac{p - p_o}{6\eta\omega}\left(\frac{c^2}{R^2}\right)$$

$x = r\theta$

$Z = z/L$

$H = h/c$

ε_r: the eccentricity ratio

H: film thickness

P: pressure

3.0 JOURNAL DEVIATIONS (MISALIGNMENT)

Misalignment decreases the lubricant thickness and increases the pressure levels as explained previously. The deviation in the parallelism between the shaft and the bearing axes results in misalignment. In general, misalignment (axes deviation) occurs in horizontal, vertical, or both planes (3D misalignment). Figure 1 illustrates the 3D misalignment where δv is the vertical deviation and δh represents the horizontal deviation which varies with z axis (along bearing width). The maximum deviations ($\delta vmax, \delta h$max) which occur at the bearing edges, are used to study the 3D misalignment effect on the characteristics of the journal-bearing system.

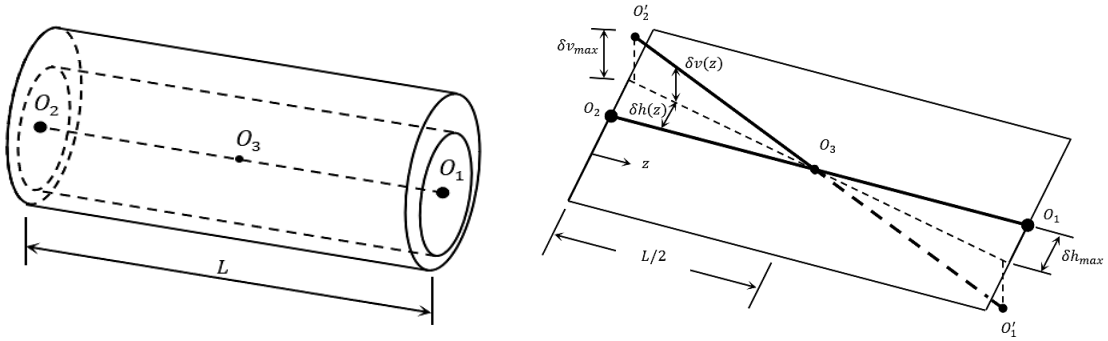

(a) (b)

Figure 1: Solution model. (a) Journal bearing, and (b) axes deviations.

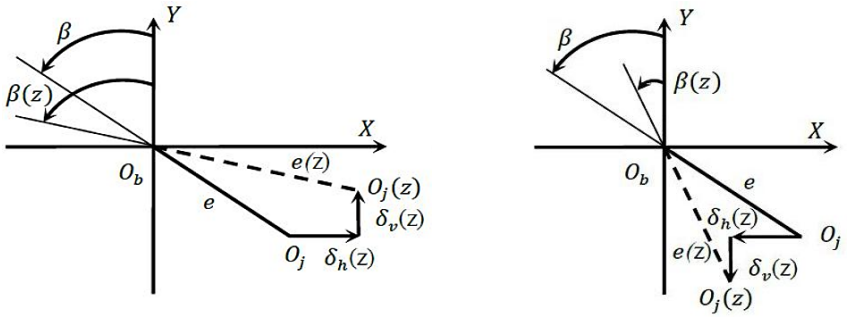

(a) (b)

Figure 2: Center deviation. (a) ($z \leq L/2$) and (b) ($z > L/2$) [21].

Figure 2 shows journal center deviation due to misalignment. Therefore, the vertical and horizontal misalignment can be given by (Jamali and Al-Hamood, 2018):

$$\begin{aligned} \delta v(z) &= \delta v_{max}\ (1.0 - 2z/L)\ \ for\ (z \leq\ 0.5L) \\ \delta v(z) &= \delta v_{max}\ (2z/L - 1.0q)\ \ for\ (z >\ 0.5L) \\ \delta h(z) &= \delta h_{max}\ (1.0 - 2z/L)\ \ for\ (z \leq\ 0.5L) \\ \delta h(z) &= \delta h_{max}\ (2z/L - 1.0)\ \ for\ (z >\ 0.5L) \end{aligned} \tag{5}$$

The two parameters are scaled (dimensionless) to the radial clearance C to give an indication of the amount of misalignment in comparison with the clearance. Therefore, using the dimensionless form, the above equations can be written as:

$$\begin{aligned} \Delta v\ (z) &= \Delta v_{max}\ (1.0 - 2Z)\ \ for\ (Z \leq\ 0.5) \\ \Delta v\ (z) &= \Delta v_{max}\ (2Z - 1.0)\ \ for\ (Z >\ 0.5) \\ \Delta h\ (z) &= \Delta h_{max}\ (1.0 - 2Z)\ \ for\ (Z \leq\ 0.5) \\ \Delta h\ (z) &= \Delta h_{max}\ (2Z - 1.0)\ \ for\ (Z >\ 0.5) \end{aligned} \tag{6}$$

where, $Z{=}z/L$ and $\Delta{=}\delta/C$: dimensionless misalignment. More details about the 3D model of misalignment used in this study can be found in Jamali and Al-Hamood, 2018.

4.0 BEARING DESIGN

Modification of the bearing width is used to avoid the lubricant thickness thinning under severe levels of misalignment and to reduce the pressure levels as explained previously. Two forms of modifications are used in this work which are second-order curve and linear modifications. The first form (curve) is shown in Figure 3. The modification is performed along a distance Zo at a height Cr where the effectiveness of modification on the performance of the bearing is evaluated based on these parameters. The general equations of modification are:

$$F(Z) = \frac{f(z)}{c} = Cr\ (\frac{1}{Zo^2}\ Z^2 - \frac{2}{Zo}Z + 1) \qquad \text{when } Zo \leq 1/2 \tag{7}$$

$$F(Z) = \frac{f(z)}{c} = \frac{Cr}{Zo^2}\ (\ Z^2 -\ 2(1 - Zo)Z + (1 - Zo)^2\ ) \qquad \text{when } Zo > 1/2 \tag{8}$$

The second form of chamfer (Linear) is shown in Figure 4. The general equations of modifications are:

$$F(Z) = \frac{f(z)}{c} = Cr(1 - \frac{1}{Zo}Z) \qquad \text{when } Zo \leq 1/2 \tag{9}$$

$$F(Z) = \frac{f(z)}{c} = Cr(\frac{1}{Zo}\ (Z - 1) + 1) \qquad \text{when } Zo > 1/2 \tag{10}$$

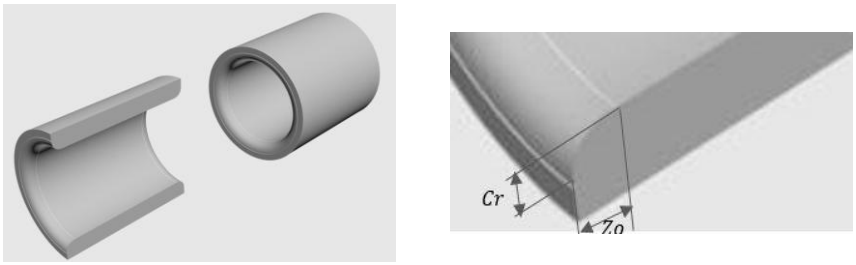

Figure 3: First form of the axial profile modification (curved chamfer).

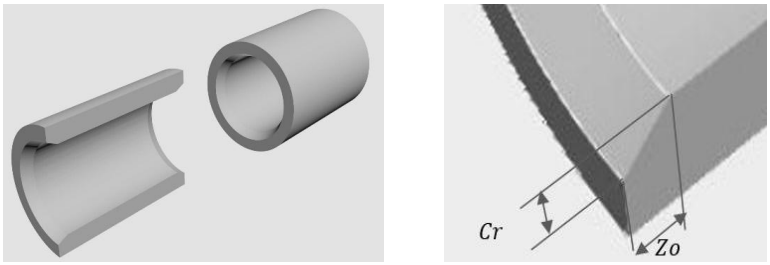

Figure 4: Second form of the axial profile modification (linear chamfer).

The parameters *Zo* and *Cr* described in Equations (7) to (10) are dimensionless where $Zo=zo/L$ and $Cr=cr/C$. Figure 5 compares the curved and linear chamfer of the modified bearing (inner surface of the bearing) for both sides of the bearing when Cr = 0.3 and Zo = 0.3. Using the curved form ensures that the modification starts at a zero slope in comparison with a sudden change in the profile when the linear form of modification is considered.

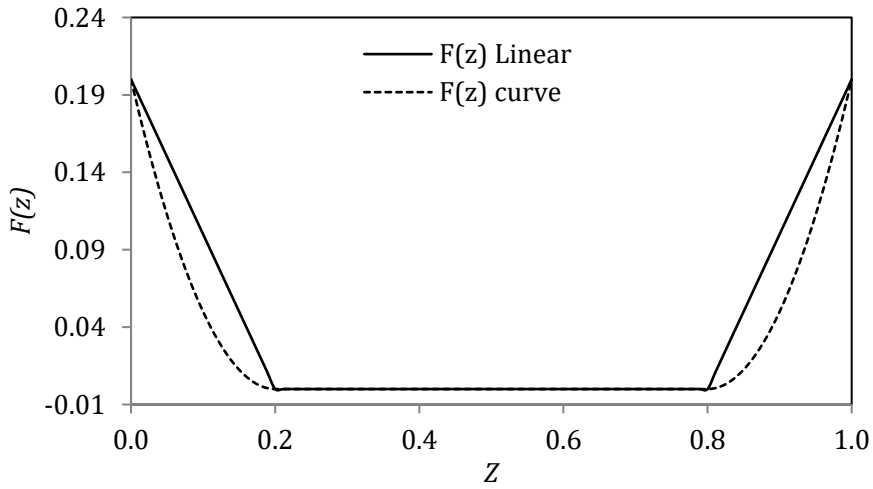

Figure 5: Curved and linear chamfer of the bearing inner surface ($F(z)$ and Z are dimensionless).

5.0 SOLUTION OF THE MATHEMATICAL MODEL

The discretization of the pressure gradients is illustrated in Figure 6 which can be given by (for the circumferential direction):

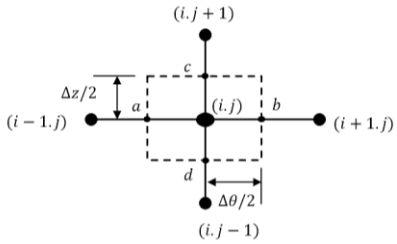

Figure 6: Finite difference discretization.

$$\frac{\partial}{\partial\theta}\left(H^3\frac{\partial P}{\partial\theta}\right) = \frac{H^3\frac{\partial P}{\partial\theta}|_b - H^3\frac{\partial P}{\partial\theta}|_a}{\Delta\theta} \tag{11}$$

$$\frac{\partial P}{\partial\theta}|_b = \frac{P_{(i+1.j)} - P_{(i.j)}}{\Delta\theta}$$
$$\frac{\partial P}{\partial\theta}|_a = \frac{P_{(i.j)} - P_{(i-1.j)}}{\Delta\theta} \tag{11-a}$$

$$H^3|_b = \left[\frac{H_{(i+1.j)} + H(i.j)}{2}\right]^3$$
$$H^3|_a = \left[\frac{H_{(i.j)} + H(i-1.j)}{2}\right]^3 \tag{11-b}$$

$$\frac{\partial H}{\partial\theta} = \frac{H_{(i+1.j)} - H(i-1.j)}{2\Delta\theta} \tag{12}$$

Similarly,

$$\frac{R^2\partial}{L^2\partial x}\left(H^3\frac{\partial P}{\partial Z}\right) = \frac{R^2}{L^2}\left[\frac{H^3\frac{\partial P}{\partial Z}|_c - H^3\frac{\partial P}{\partial Z}|_d}{\Delta Z}\right]$$
$$\frac{\partial P}{\partial Z}|_c = \frac{P_{(i.j+1)} - P_{(i.j)}}{\Delta Z} \tag{13}$$

$$\frac{\partial P}{\partial Z}|_d = \frac{P_{(i.j)} - P_{(i.j-1)}}{\Delta Z} \tag{13-a}$$

$$H^3|_c = \left[\frac{H_{(i.j+1)} + H(i.j)}{2}\right]^3$$
$$H^3|_d = \left[\frac{H_{(i.j)} + H(i.j-1)}{2}\right]^3 \tag{13-b}$$

Substituting these equations in Equation (3) results in:

$$P_{(i.j)} = \frac{1}{\gamma}\left[{H_b}^3\, P_{(i+1.j)} + {H_a}^3\, P_{(i-1.j)} + B_1B_2{H_c}^3\, P_{(i.j+1)} + B_1B_2{H_d}^3\, P_{(i.j-1)} - C_1H_{(i+1.j)} + C_1H_{(i-1.j)}\right] \quad (14)$$

where;

$$B_1 = \frac{R^2}{L^2}$$
$$B_2 = \frac{d\theta^2}{dz^2}$$
$$C_1 = \frac{d\theta}{2}$$
$$\gamma = {H_b}^3 + {H_a}^3 + B_1B_2{H_c}^3 + B_1B_2{H_d}^3$$

The load components are given by:

$$Wt = \int_0^1 \int_0^{\theta_{cav}} P\ sin\,\theta\ RLd\theta\ dz$$
$$Wt = \int_0^1 \int_0^{\theta_{cav}} P\ sin\,\theta\ RLd\theta\ dz$$
$$W = \sqrt{{W_t}^2 + {W_r}^2} \quad (15)$$

The Reynolds boundary conditions method is used to determine θ_{cav}. The attitude angle is:

$$\beta = \tan^{-1}\frac{W_t}{W_r} \quad (16)$$

6.0 LINEAR STABILITY ANALYSIS

The equations of motion for the rotor shown in Figure 7 which is supported by two journal bearings are (Tieu and Qiu, 1995):

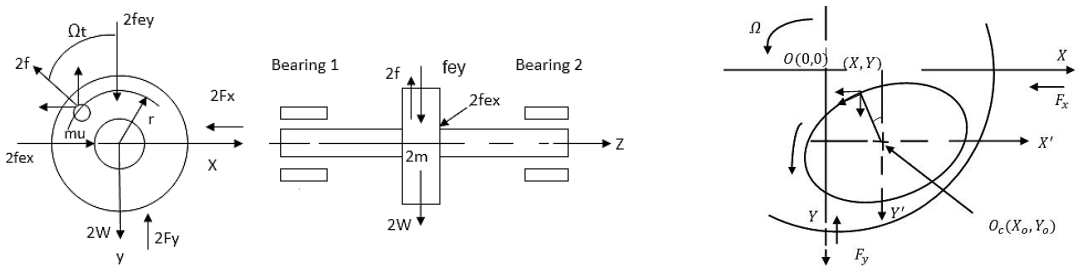

(a) (b)

Figure 7: Rigid rotor and its supports. (a) Schematic drawing of the system, and (b) Journal movement (Coordinate system) (Tieu and Qiu, 1995).

$$m\,\ddot{x}' = -Fx + f_{ex} - f\sin\Omega t \tag{17}$$

$$m\,\ddot{y}' = -Fy + f_{ey} - f\cos\Omega t + W \tag{18}$$

The derivative in these equations can be given by:

$$\ddot{x}' = \frac{d^2x'}{dt^2} = \frac{d^2(X'C)}{d(t^2/\Omega^2)} = C\Omega^2 * \frac{d^2X'}{dT^2} = C\Omega^2\,\ddot{X}'$$

$$\ddot{y}' = \frac{d^2y'}{dt^2} = \frac{d^2(Y'C)}{d(T^2/\Omega^2)} = C\Omega^2 * \frac{d^2Y'}{dT^2} = C\Omega^2\,\ddot{Y}'$$

where:

$x' = X'\,C$
$y' = Y'\,C$
$\Omega t = T$

Substitute $\ddot{x}' = C\Omega^2\,\ddot{X}'$ in Equation (17) yields:

$$\ddot{X}' = \frac{1}{\mathrm{mC}\Omega^2} * (-Fx + f_{ex} - m_u\,\mathrm{r}\,\Omega^2\sin\Omega t) \tag{19}$$

Equation (19) can be written as:

$$\ddot{X}' = \frac{1}{\overline{\mathrm{M}}} * (-\bar{\mathrm{F}}x + \bar{\mathrm{F}}_{ex} - \overline{\mathrm{Ru}}\sin\mathrm{T}) \tag{20}$$

where:

$$\bar{M} = \frac{m\,C\,\Omega^2}{W}$$
$$\bar{F}x = \frac{Fx}{W}$$
$$\bar{\mathrm{F}}_{ex} = \frac{f_{ex}}{W}$$
$$\overline{\mathrm{Ru}} = m_u\,\mathrm{r}\frac{\Omega^2}{\mathrm{W}}$$

A similar procedure can be followed for $\ddot{Y}'$ which gives:

$$\ddot{Y}' = \frac{1}{\overline{\mathrm{M}}} * \left(-\bar{\mathrm{F}}\mathrm{y} + \bar{\mathrm{F}}_{ey} - \overline{\mathrm{Ru}}\cos\mathrm{T} + 1\right) \tag{21}$$

Equations (20) and (21) can be given by:

$$\bar{M}\ddot{X}' = -\bar{\mathrm{F}}x + \bar{\mathrm{F}}_{ex} - \overline{\mathrm{Ru}}\sin\mathrm{T}$$
$$\bar{M}\ddot{Y}' = -\bar{\mathrm{F}}\mathrm{y} + \bar{\mathrm{F}}_{ey} - \overline{\mathrm{Ru}}\cos\mathrm{T} + 1 \tag{22}$$

The standard linear forms of the equations that are used to calculate the critical speed of the system are identified by neglecting the unbalance and external loads as follows:

$$\bar{M}\ddot{X}' + \bar{F}x = 0$$
$$\bar{M}\ddot{Y}' + \bar{F}y = 0 \quad (23)$$

where:

$$\bar{F}x = K_{xx}\,X' + K_{xy}\,Y' + C_{xx}\,\dot{X}' + C_{xy}\,\dot{Y}' \quad (24)$$

$$\bar{F}y = K_{yx}\,X' + K_{yy}\,Y' + C_{yx}\,\dot{X}' + C_{yy}\,\dot{Y}' \quad (25)$$

The dynamic coefficients are given by:

$$K_{xx} = \int_0^1 \int_0^{2\pi} P_x\ cos\ \theta\ d\theta\ dz$$
$$K_{xy} = \int_0^1 \int_0^{2\pi} P_y\ cos\ \theta\ d\theta\ dz$$
$$K_{yx} = \int_0^1 \int_0^{2\pi} P_x\ sin\ \theta\ d\theta\ dz$$
$$K_{yy} = \int_0^1 \int_0^{2\pi} P_y\ sin\ \theta\ d\theta\ dz \quad (26)$$

$$C_{xx} = \int_0^1 \int_0^{2\pi} P_{\dot{x}}\ cos\ \theta\ d\theta\ dz$$
$$C_{xy} = \int_0^1 \int_0^{2\pi} P_{\dot{y}}\ cos\ \theta\ d\theta\ dz$$
$$C_{yx} = \int_0^1 \int_0^{2\pi} P_{\dot{x}}\ sin\ \theta\ d\theta\ dz$$
$$C_{yy} = \int_0^1 \int_0^{2\pi} P_{\dot{y}}\ sin\ \theta\ d\theta\ dz \quad (27)$$

where: P_x, P_y, $P_{\dot{x}}$ and $P_{\dot{y}}$ are the pressure derivatives with respect to X, Y, $\dot{X}$ and $\dot{Y}$, respectively, and the integrals into Equations (26) and (27) are calculated numerically. Substitution of Equations (24) and (25) into Equation (23) gives:

$$\bar{M}\,\ddot{X}' + K_{xx}\,X' + K_{xy}\,Y' + C_{xx}\,\dot{X}' + C_{xy}\,\dot{Y}' = 0$$
$$\bar{M}\,\ddot{Y}' + K_{yx}\,X' + K_{yy}\,Y' + C_{yx}\,\dot{X}' + C_{yy}\,\dot{Y}' = 0 \quad (28)$$

Let $X' = \mathrm{A}e^{i\lambda t}$ and $Y' = \mathrm{B}e^{i\lambda t}$. The derivatives become:

$$\ddot{X}' = -\lambda^2 \mathrm{A}e^{i\lambda t}$$
$$\ddot{Y}' = -\lambda^2 \mathrm{B}e^{i\lambda t} \quad (29)$$

Substitution of Equation (29) into Equation (28) yields:

$$(-(\bar{M}\,\lambda^2 - K_{xx}) + i\lambda\, C_{xx})A + \left(K_{xy} + C_{xy} i\lambda\right)B = 0$$
$$\left(-\left(\bar{M}\,\lambda^2 - K_{yy}\right) + i\lambda\, C_{yy}\right)B + \left(K_{yx} + C_{yx} i\lambda\right)A = 0$$

The nontrivial solution requires:

$$\begin{vmatrix} -(\bar{M}\,\lambda^2 - K_{xx}) + i\lambda C_{xx} & K_{xy} + C_{xy} i\lambda \\ K_{yx} + C_{yx} i\lambda & -\left(\bar{M}\,\lambda^2 - K_{yy}\right) + i\lambda\, C_{yy} \end{vmatrix} = 0$$

which is simplified to:

$$\begin{aligned} (\bar{M}\,\lambda^2 - K_{xx})\left(\bar{M}\,\lambda^2 - K_{yy}\right) - (\bar{M}\,\lambda^2 - K_{xx}) i\lambda\, C_{yy} - \left(\bar{M}\,\lambda^2 - K_{yy}\right) i\lambda\, C_{xx} \\ - \lambda^2\, C_{xx}\, C_{yy} - K_{xy}\, K_{yx} - K_{yx}\, C_{xy} i\lambda - K_{xy}\, C_{yx} i\lambda \\ + \lambda^2\, C_{xy} C_{yx} = 0 \end{aligned}$$

Equating the real part to zero gives:

$$\lambda = \sqrt{\frac{(keq - K_{xx})\left(keq - K_{yy}\right) - K_{xy}\, K_{yx}}{C_{xx}\, C_{yy} - C_{xy} C_{yx}}} \tag{30}$$

where, $\bar{M}\,\lambda^2 = keq$ (is the equivalent stiffness) and λ is the whirl frequency ratio. Similarly, equating the imaginary part to zero yields:

$$keq = \frac{K_{xx}\, C_{yy} + K_{yy} C_{xx} - K_{yx}\, C_{xy} - K_{xy}\, C_{yx}}{C_{xx} + C_{yy}} \tag{31}$$

Therefore, the critical speed is:

$$\Omega_{crit} = \frac{\sqrt{keq}}{\lambda} \tag{32}$$

The pressure field and lubricant thickness are determined by solving the governing equations and incorporating the 3D misalignment model with the equations of profile modification using successive over-relaxation method. After that, the dynamic coefficients are determined using numerical integration to determine the stability limits. An overview of the solution method is illustrated in Figure 8.

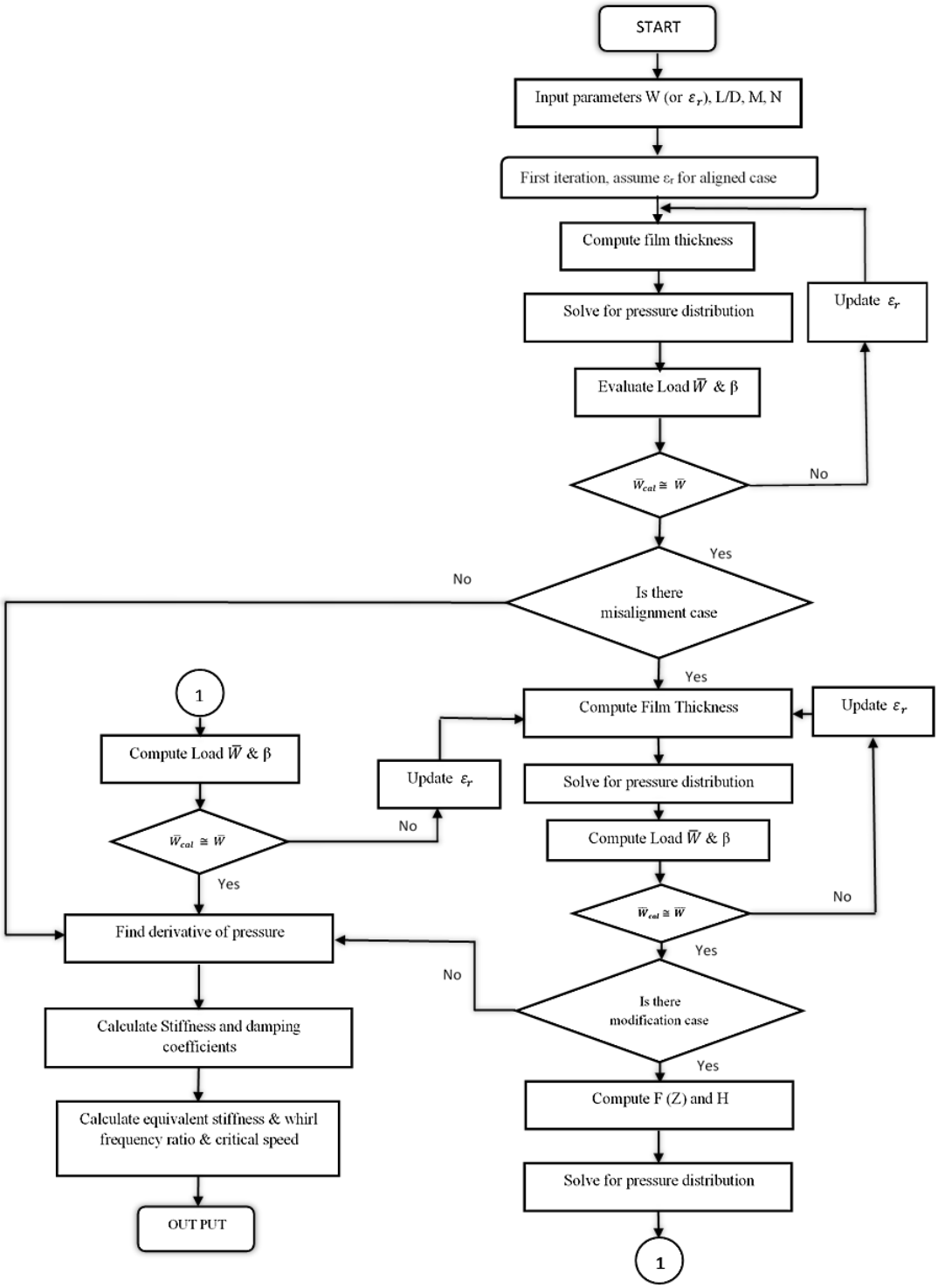

Figure 8: Flow chart of the solution strategy.

7.0 RESULTS AND DISCUSSIONS

The presented results in this work cover the bearing modification considering the wide range of chamfer parameters (Zo, Cr). The number of mesh points ($k = M \times N$) used in this work is 16471 points, where a series of tests is examined to ensure the independence of the outcome on k. Some of the results of the current solution (P_{max} and θ_{cav}) are compared with the work of Khonsari and Booser, 2017 using different ε_r and L/D ratios as shown in Table 1. The maximum differences in P_{max} and θ_{cav} are only 0.59% and 1.01%, respectively.

Table 1: Current work results vs. the work of Khonsari and Booser, 2017 for different L/D ratios.

L/D	ε_r	θ_{cav} Current	P_{max} Current	θ_{cav} Reference [24]	P_{max} Reference [24]
2	0.25	226	08.4579	225	08.4574
2	0.45	218	18.5553	216	18.5628
2	0.65	208	40.0587	207	39.8234
1.5	0.25	220	06.4996	219	06.4996
1.5	0.45	214	15.0571	213	15.0641
1.5	0.65	206	34.7622	207	34.8108
1	0.25	212	03.9503	210	03.9506
1	0.45	208	09.9250	207	09.9301
1	0.65	202	25.9088	204	25.9119
0.5	0.25	198	01.3143	198	01.3144
0.5	0.45	196	03.7178	198	03.7169
0.5	0.65	196	11.7469	195	11.7537

Furthermore, the critical speeds are also validated against the well-known solution of Lund and Thomsen, 1978 when $L/D = 1/2$ and $L/D = 1.0$ as shown in Figure 9. The two sets of results are very close where the max difference is only 0.11 %.

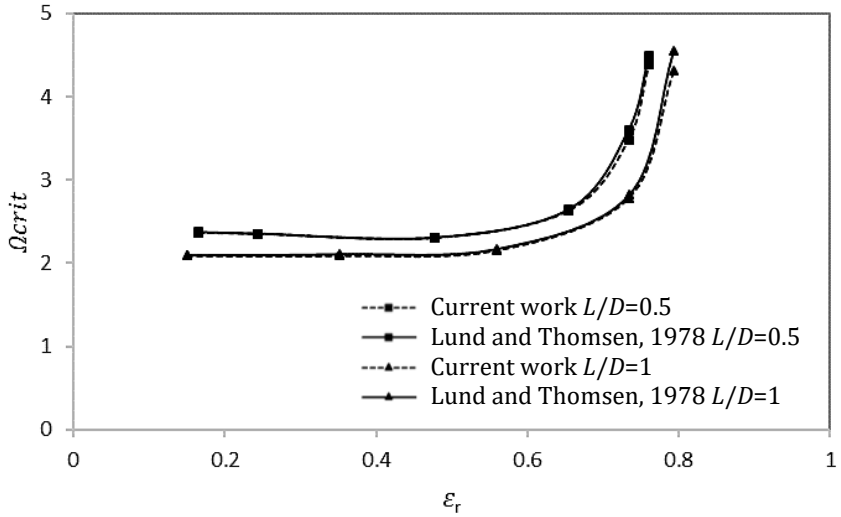

Figure 9: Comparison between the current work and the established work (Lund and Thomsen, 1978) $at\ L/D = 1/2$ and $L/D = 1.0$ for the dimensionless critical speed (Ω_{crit}).

Figure 10 illustrates 3D and 2D pressure contours for four cases which are aligned, misaligned, and modified bearing using linear and second-order forms of modification (Zo = 0.3 and Cr = 0.3). The dimensionless max pressure for the ideal case is 1.1842. For the second case (misaligned), the maximum pressure is 1.8138 which represents an increase of 53 % in the pressure value. In the third case (curved chamfer) the pressure value reduces to 1.433 (21 % reduction) and in the last case (linear chamfer), P_{max} is 1.4778 which means a reduction of 18.5 % in P_{max}. The results in these four cases are converged to the same applied load, and the pressure distributions are shifted (for the purpose of presentation only) in such a way that in all cases the reference axis ($\theta = 0$) is the line of centers (along the eccentricity) in order to make a clear comparison with the aligned case. In addition, the film thicknesses for these four cases are shown in Figure 11. The minimum film thicknesses in these cases are 0.3, 0.055, 0.198 and 0.2078, respectively. These results show that the misalignment causes a reduction in H_{min} of 80% and the two forms of modification resulted in an increase of 261 % and 277 % in H_{min} , respectively relative to deviation case. The values of chamfer factors used in this figure (Zo = 0.3 and Cr = 0.3) give almost the same results regardless of the form of chamfer used in the modification of the inner surface of the bearing. However, using higher values increases the difference between the results of the two forms of modification as shown in Figure 12.

Figure 13 illustrates the effect of chamfer parameters (Zo, Cr) on P_{max} and H_{min} using the two forms of modification. The horizontal green lines in this figure are used to represent the aligned unmodified bearings. The misalignment parameters used to produce the other results in this figure are $\Delta h_{max} = \Delta v_{max} = 0.52$. These values reduce the film thickness significantly, therefore it was used as an extreme case of 3D misalignment. Figure 13a shows the results of the case of curved modification. The range of Zo is 0 – 0.5 where Zo = 0 means that the profile is without modification while when Zo = 0.5, the whole bearing width is modified (half the bearing width from each side). The values of Cr are in the range of 0 – 2 where, Cr = 0 implies no change in the bearing profile, and Cr = 2 means that the height of modification is twice the designed clearance. The max. pressure is 1.814 for the unmodified misaligned case. Adopting the axial profile modification with $Zo \leq 1/2$, P_{max} decreases below this value when Cr < 0.5. On the other hand, when $Cr \geq 0.5$, P_{max} increases significantly above this value, in particular, when Zo > 0.3. Therefore, the high value of Cr must be avoided. For the deviation case, H_{min} is 0.055. It is clear that the profile modification enhances H_{min} for the whole range of Zo in comparison with the misalignment case. The minimum film thickness continues to rise when Cr < 0.5. Therefore, it can be concluded that the recommended limits of Zo and Cr are Zo < 0.5 and Cr < 0.5. Figure 13b illustrates the results of the linear modification. The general behavior is similar to that of curved chamfer for the lower values of Zo and Cr. The levels of P_{max} are higher when Zo > 0.3 and H_{min} values are lower when Zo > 0.3. Nevertheless, this case required more investigation regarding the possibility of producing a considerable elastic deformation due to misalignment. The slop discontinuity of the profile due to the linear modification may have negative consequences on the levels of pressure if the bearing deformation at this position is considered.

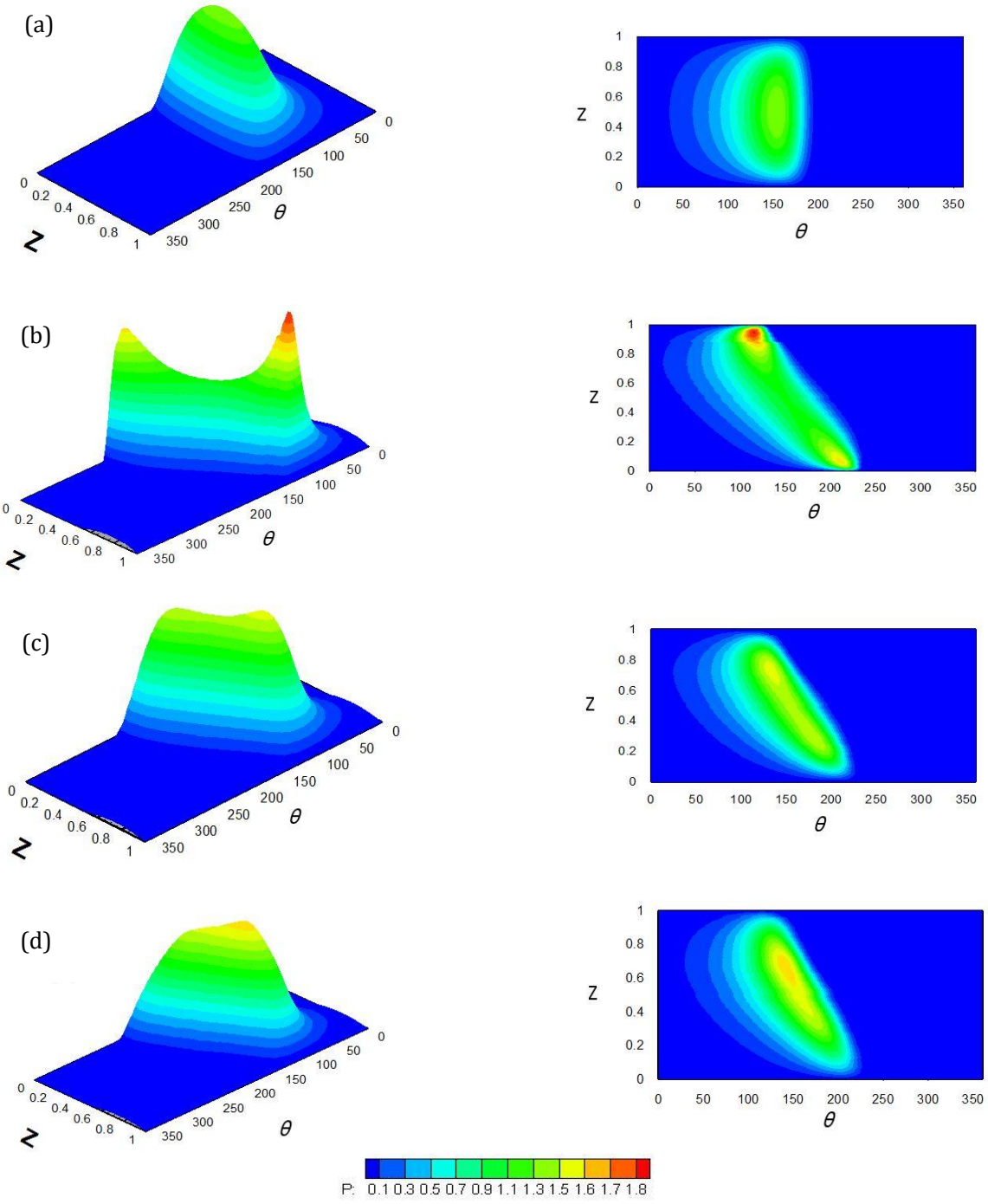

Figure 10: Pressure distribution (left: 3D, right: 2D). (a) aligned, (b) misaligned, (c) misaligned and curve modification and (d) misaligned and linear modification. (L/D = 1.5, Zo = 0.3, Cr = 0.3).

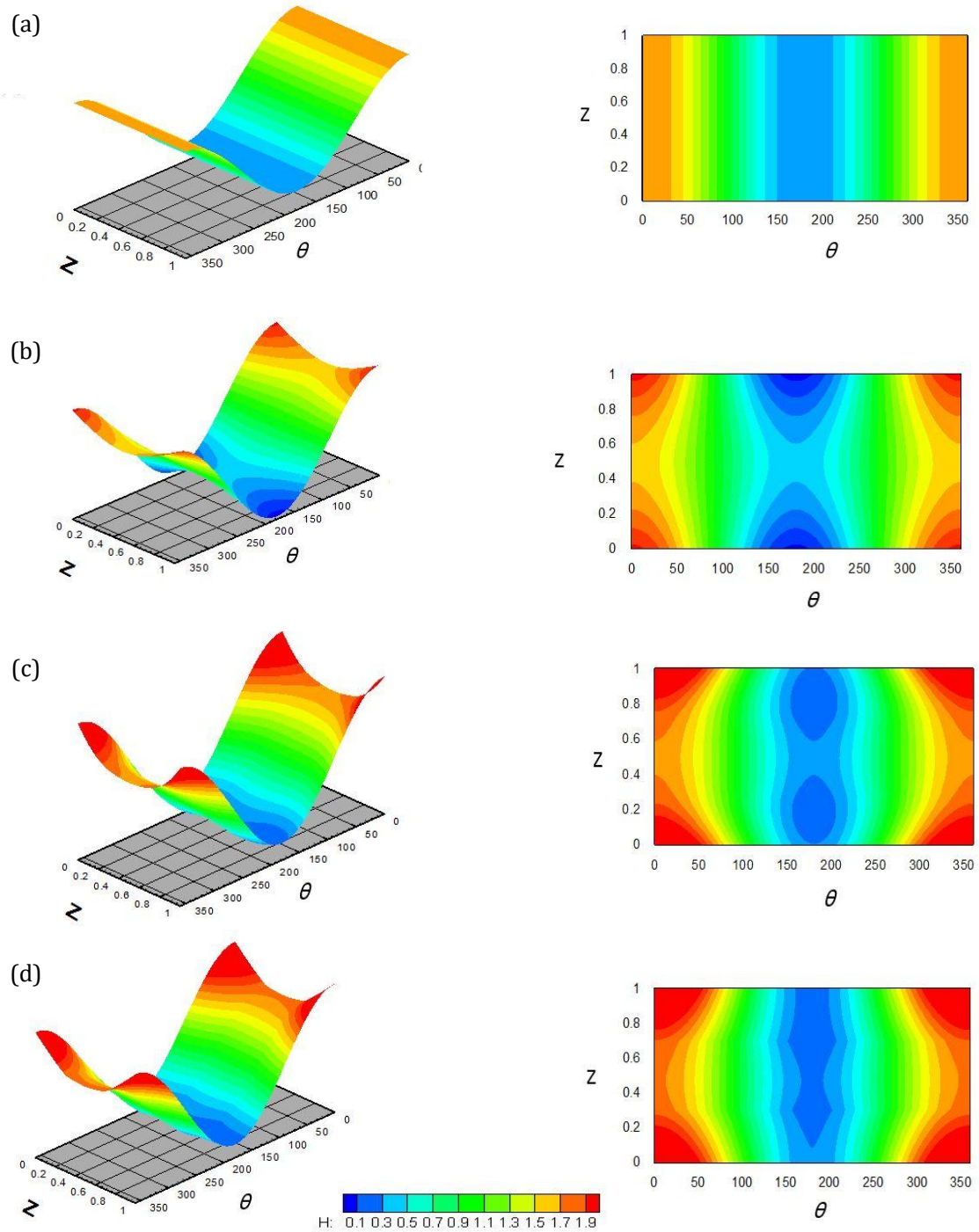

Figure 11: Film thickness (left: 3D, right: 2D). (a) aligned, (b) misaligned, (c) misaligned and curve modification and (d) misaligned and linear modification. (L/D = 1.5, Zo = 0.3, Cr = 0.3).

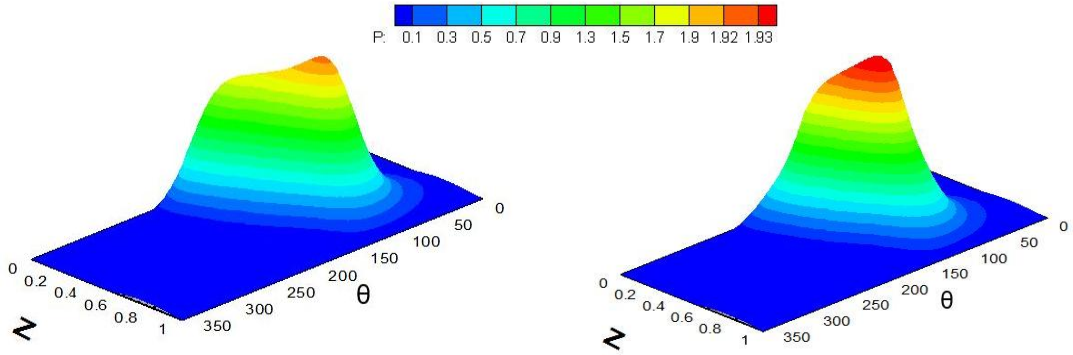

Figure 12: 3D pressure distribution of misaligned journal bearings (a) curved modification (b) linear modification (L/D =1.5, Zo = 0.3, Cr = 0.5).

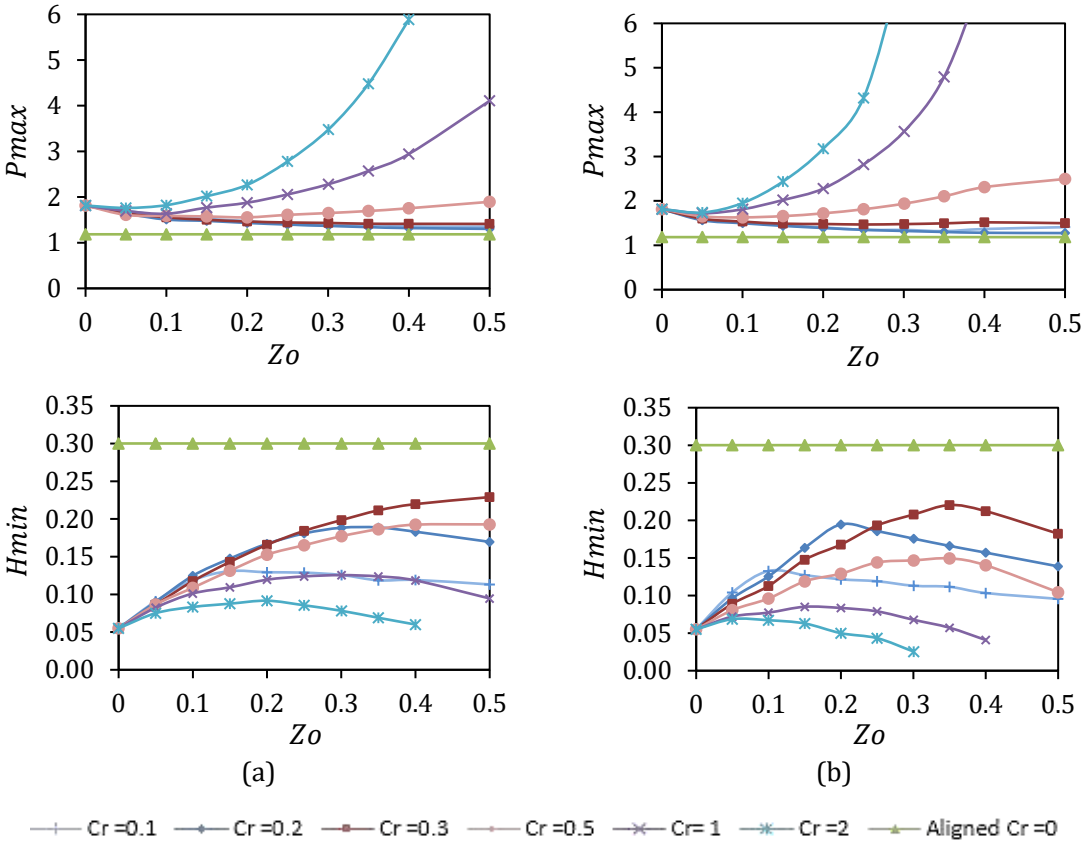

Figure 13: Effect of chamfer parameters on P_{max} and H_{min}. (a) Left side: curved modification and (b) right side: linear modification. (L/D =1.5, Δh_{max}= Δv_{max} = 0.52 and ε_r = 0.7).

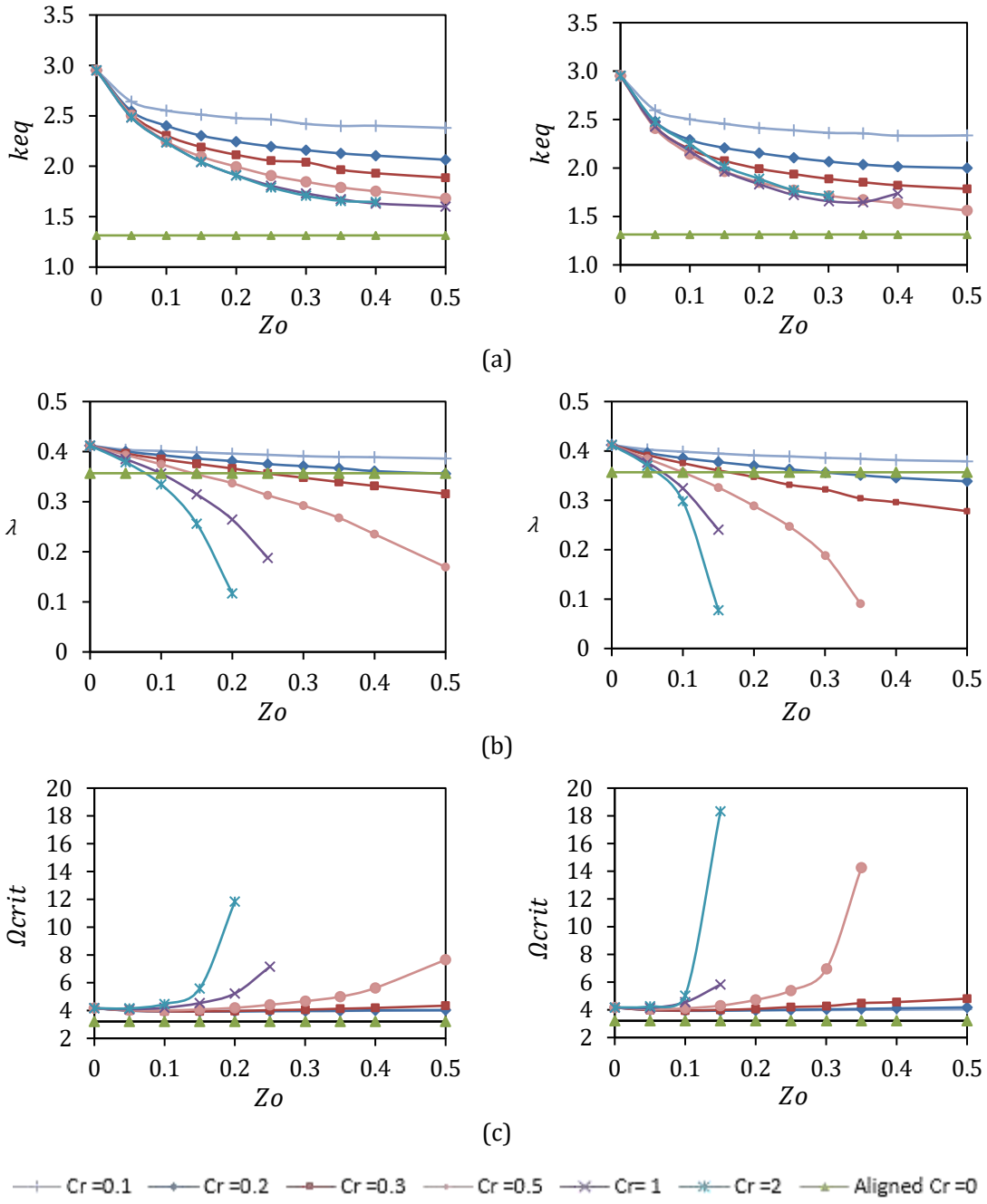

Figure 14: Effect of modification on dynamic characteristics. Left side: curved modification and the right side: Linear modification. (a) Equivalent stiffness keq, (b) Critical whirl frequency ratio λ and (c) critical speed Ω_{crit} (L/D = 1.5, $\Delta h_{max} = \Delta v_{max}$= 0.52, ε_r= 0.7).

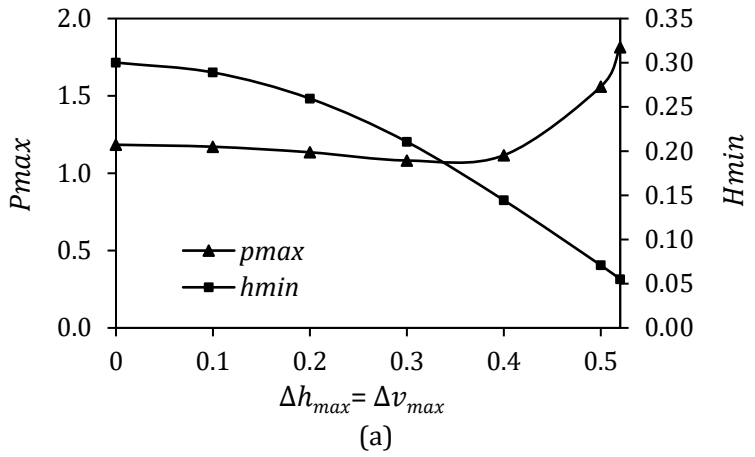

Figure 15: Effect of 3D misalignment (Δh_{max} and Δv_{max}) on (a) P_{max} and H_{min}, (b) Keq and (c) Ω_{crit}.

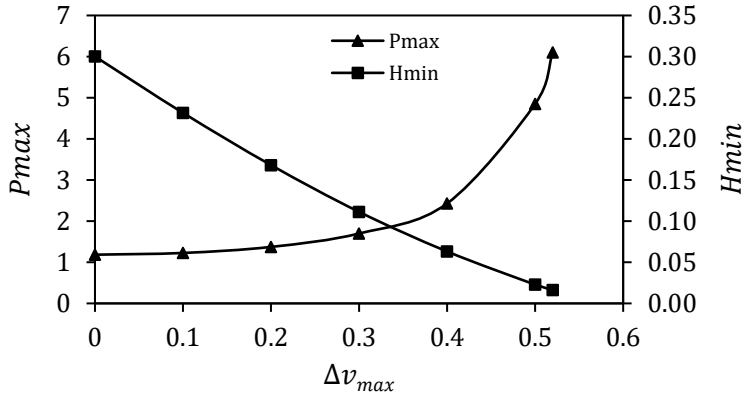

(a)

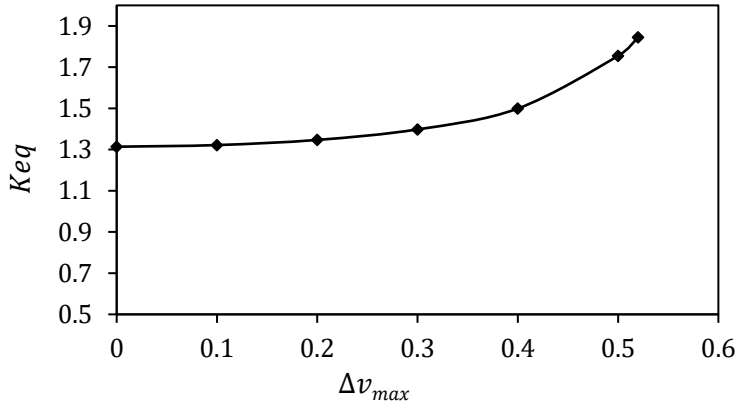

(b)

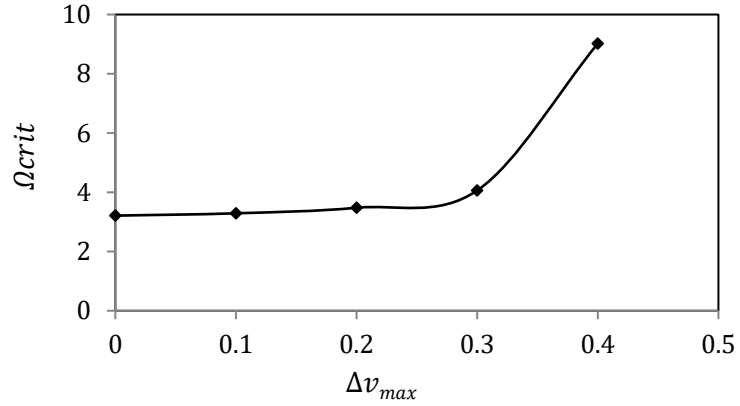

(c)

Figure 16: Effect of vertical misalignment (Δh_{max}= 0) on (a) P_{max} and H_{min}, (b) Keq and (c) Ω_{crit}.

Figure 14 illustrates the form of modification effect on keq, λ and Ω_{crit} using a wide range of chamfer parameters. The left and right side of Figure 14 illustrates the linear form of the chamfer respectively. Figures 14(a) and 14(b) illustrate the variation in keq and λ respectively. It is clear that all values of chamfer factors (Cr, Zo) have obvious effects on keq and λ. These effects would be easy to interpret in terms of the critical speed that is shown in Figure 14(c). Figure 14(c) illustrates the variation in critical speed with (Zo, Cr) for the two forms of chamfer. The range of Zo is (0 - 0.5) and (0 – 2) for Cr. The case of a perfectly aligned and unmodified bearing is illustrated by the horizontal green line. Ω_{crit} , in the case of deviation is 4.169, while it is 3.212 in the aligned case which means that the critical speed is 29.7 % greater. However, the maximum pressure in the case of misaligned is more than in the case of aligned and H_{min}, also reduces significantly because of misalignment which affects the bearing carrying. Therefore, to ensure acceptable levels of H_{min} and P_{max} values without sacrificing the enhancement in Ω_{crit}, the modification is used. Ω_{crit} in the case of curve modification is 4.06, and the value of Ω_{crit} in the case of linear modification is 4.269 when Zo=0.3 and Cr=0.3. This means an increase of 26.4 % and 32.9 % in Ω_{crit} for the curved and linear modification respectively. Higher value of Ω_{crit} are obtained when Cr > 0.3 and Zo > 0.3 but these ranges are not the best from H_{min} and P_{max} point of view as explained previously.

Figure 15 illustrates the 3D misalignment consequences (horizontal and vertical misalignment) on P_{max}, H_{min}, keq and Ω_{crit} for a wide range of Δh_{max}, Δv_{max}. The misaligned increases maximum pressure, equivalent stiffness, critical whirl frequency ratio and critical speed decreases minimum film thickness when $\Delta h_{max} = \Delta v_{max} > 0.2$.

Figure 16 shows the effect of vertical misalignment ($\Delta h_{max} = 0$) on P_{max} ,H_{min} , keq and Ω_{crit}. The vertical misalignment (Δv_{max}) in this figure varies from 0 to 0.52. It is clear that the effects of vertical misalignment on the considered results are similar to the effects of 3D misalignment shown in Fig. 15, where a higher misalignment value increases P_{max} , keq and Ω_{crit} and reduces H_{min} , particularly when $\Delta v_{max} > 0.2$.

8.0 CONCLUSION

In this work, a comprehensive analysis is presented of the bearing modification and its effects on the journal bearing performance. The change in the design of the bearing inner surface is performed using two types of modification which are linear and second order curve. The solution also considered a 3D misalignment (deviation) model in this analysis. The mathematical model is solved numerically using finite different methods considering the Reynolds boundary condition method to determine iteratively the position of the cavitation angle. The investigation includes the modification effects on the levels of pressure and lubricant thickness in addition to its effect on the stability threshold of the bearing system. The results showed that the deviations between the shaft and bearing axes result in a significant drop in the gap between the shaft and bearing inner surface. This reduction increases the pressure levels significantly close to the edge of the bush. Using the second order profile, where the slop continuity is maintained, for the modification reduces the pressure spikes resulting in due to misalignment by 21%, increases the levels of film thickness by 261%, and improves the system stability where the critical speed remains higher than the corresponding value of the perfectly aligned bearing. The slop discontinuity of the profile due to the linear profile may have negative consequences on the levels of pressure if the bearing deformation at this position is considered. Therefore, further investigation is required regarding

the possibility of producing a considerable elastic deformation due to misalignment at the start of the linear profile.

LIST OF ABBREVIATIONS

C	Bearing radial clearance	m
cr	Chamfer height	m
Cr	Dimensionless chamfer height	-
$C_{xx}, C_{xy}, C_{yx}, C_{yy}$	Dimensionless dynamic coefficients	-
e	Eccentricity of journal	m
f_{ex} , f_{ey}	Half external forces	N
$\bar{F}_{ex}, \bar{F}_{ey}$	Dimensionless half external forces	-
$\bar{\mathrm{F}}$x , $\bar{\mathrm{F}}$y	Dimensionless bearing force	-
h	Film thickness	m
H	Dimensionless film thickness, $H = \frac{h}{c}$	-
H_{min}	Dimensionless minimum film thickness	-
k	Total number of points	-
keq	Equivalent stiffness	-
K_{xx} , K_{xy}, K_{yx}, K_{yy}	Dimensionless stiffness coefficients	-
L	Bearing length	m
M	No. of points in axial direction	-
m	Rotor mass half	kg
m_{u}	Unbalance mass	kg
$\bar{M}$	Dimensionless half rotor mass	-
N	No. of points in circumferential direction	-
O_{b}	Bearing center	-
O_{j}	Journal center	-
P_{max}	Dimensionless maximum pressure	-
$\bar{P}$	Derivative of pressure (dimensionless)	-
P	Non-dimensional pressure	-
R	Bearing radius	m
$\overline{Ru}$	Dimensionless unbalance force	-
t	Time	Second
T	Dimensionless time	-
W	Total load	N
W_r	Radial component of the load	N
W_t	Tangential component of the load	N
$\bar{W}$	Non-dimensional total load	-
$\acute{x}$, $\acute{y}, x, y$ z	Coordinates	m
Z	Non-dimensional coordinate, $\mathrm{Z} = \frac{Z}{L}$	-
zo	Chamfer length	m
Zo	Non-dimensional chamfer length	-

NOMENCLATURE

ε_r	Eccentricity Ratio	-
η	viscosity	Pa. s
θ_{cav}	Angle of cavitation	deg.
β	Attitude angle	deg.
ω	Angular velocity	rad/sec
δh_{max}	Max. horizontal misalignment at the bearing edges	m
δv_{max}	Max. vertical misalignment at the bearing edges	m
Δ	Dimensionless misalignment	-
Δh_{max}	Max. horizontal misalignment at the bearing edges (dimensionless)	-
Δv_{max}	Max. vertical misalignment at the bearing edges (dimensionless)	-
$\Delta\theta$	step in the circumferential direction	deg.
ΔZ	step in the longitudinal direction	-
λ	Critical whirl frequency ratio	-
Ω	Journal rotation speed	rad/s
Ω_{crit}	Critical speed	-

REFERENCES

Al-Dujaili, Z. A., Jamali, H. U., & Al-Saadi, M. (2020). Effect of axial profile modification on the characteristics of a finite length misaligned journal bearing. IOP Conference Series: Materials Science and Engineering, 671(1), 012021.

Al-Hamood, A., Jamali, H. U., Abdullah, O. I., Senatore, A., & Kaleli, H. (2019). Numerical analysis of cam and follower based on the interactive design approach. International Journal on Interactive Design and Manufacturing.

Chasalevris, A., & Sfyris, D. (2013). Evaluation of the finite journal bearing characteristics using the exact analytical solution of the Reynolds equation. Tribology International, 57, 216–234.

Chen, C., Jing, J., Cong, J., & Dai, Z. (2019). Identification of dynamic coefficients in circular journal bearings from unbalance response and complementary equations. Proceedings of the Institution of Mechanical Engineers, Part J: Journal of Engineering Tribology, 233(7), 1016–1028.

Ferron, J., Frene, J., & Boncompain, R. (1983). A study of the thermohydrodynamic performance of a plain journal bearing: Comparison between theory and experiments. Journal of Tribology, 105, 422–428.

Jain, D., & Sharma, S. C. (2017). Dynamic analysis of a 2-lobe geometrically imperfect journal bearing system. Proceedings of the Institution of Mechanical Engineers, Part J: Journal of Engineering Tribology, 231(7), 934–950.

Jamali, H. U., & Al-Hamood, A. (2018). New method for the analysis of misaligned journal bearing. Tribology in Industry, 40(2), 213–224.

Jamali, H. U., Al-Hamood, A., Abdullah, O. I., Senatore, A., & Schlattmann, J. (2019). Lubrication analyses of cam and flat-faced follower. Lubricants, 7(31), 1–19.

Jamali, H. U., Sharif, K., Evans, H. P., & Sindle, R. W. (2013). Analysis of elasto-hydrodynamic lubrication of helical gear tooth contacts including the effects of crowning and the form of tip relief. In Proceedings of the International Conference on Gears.

Jamali, H. U., Sharif, K. J., Evans, H. P., & Sindle, R. W. (2015). The transient effects of profile modification on elasto-hydrodynamic oil films in helical gears. Tribology Transactions, 58(1), 119–130.
Khonsari, M. M., & Booser, E. R. (2017). Applied tribology: Bearing design and lubrication (3rd ed.). John Wiley & Sons.
Lund, J. W., & Thomsen, K. K. (1978). A calculation method and data for the dynamic coefficients of oil-lubricated journal bearings. ASME.
Mehrjardi, M. Z., Rahmatabadi, A. D., & Meybodi, R. R. (2016). A comparative study of the preload effects on the stability performance of noncircular journal bearings using linear and nonlinear dynamic approaches. Proceedings of the Institution of Mechanical Engineers, Part J: Journal of Engineering Tribology, 230(7), 797–816.
Miraskari, M., Hemmati, F., Alqaradawi, M. Y., & Gadala, M. S. (2017). Linear stability analysis of finite length journal bearings in laminar and turbulent regimes. Proceedings of the Institution of Mechanical Engineers, Part J: Journal of Engineering Tribology, 231(10), 1254–1267.
Miyanaga, N., & Tomioka, J. (2019). Linear and nonlinear stability analysis of hydrodynamic journal bearings using mass-conservative cavitation model. Jurnal Tribologi, 22(a), 61–73.
Nicoletti, R. (2013). Optimization of journal bearing profile for higher dynamic stability limits. Journal of Tribology, 135, 011702.
Ogrodnik, P. J., Xu, W., Goodwin, M. J., & Bancroft, G. A. (2011). The effects of dimensional manufacturing tolerances on stability of a symmetric hydrodynamic journal bearing rotor system: An experimental investigation. Proceedings of the Institution of Mechanical Engineers, Part J: Journal of Engineering Tribology, 225(12), 1152–1158.
Papadopoulos, C. A., Nikolakopoulos, P. G., & Gounaris, G. D. (2008). Identification of clearances and stability analysis for a rotor-journal bearing system. Mechanism and Machine Theory, 43(4), 411–426.
Qiu, Z. L., & Tieu, A. K. (1995). Misalignment effect on the static and dynamic characteristics of hydrodynamic journal bearings. Journal of Tribology, 117, 717–723.
Rao, T. V. (2012). Stability characteristics of misaligned journal bearing. Advances in Vibration Engineering, 11, 361–369.
Shi, J., Cao, H., & Chen, X. (2020). Effect of angular misalignment on the dynamic characteristics of externally pressurized air journal bearing. Proceedings of the Institution of Mechanical Engineers, Part J: Journal of Engineering Tribology, 234(2), 205–228.
Strzelecki, S. (2005). Operating characteristics of heavy loaded cylindrical journal bearing with variable axial profile. Materials Research, 8(4), 481–486.
Sun, F., Zhang, X., Wang, X., Su, Z., & Wang, D. (2019). Effects of shaft shape errors on the dynamic characteristics of a rotor-bearing system. Journal of Tribology, 141(10).
Tieu, A. K., & Qiu, Z. L. (1995). Stability of finite journal bearings: From linear and nonlinear bearing forces. Tribology Transactions, 38(3), 627–635.
Xu, W., Ogrodnik, P. J., Li, B., Zhang, H., & Gao, S. (2015). Effect of journal out-of-roundness on stability of a symmetric hydrodynamic journal bearing system. Part 1: Theoretical analysis. Proceedings of the Institution of Mechanical Engineers, Part J: Journal of Engineering Tribology, 229(11), 1347–1358.
Yadav, S. K., Rajput, A. K., Ram, N., & Sharma, S. C. (2019). Stability analysis of a rigid rotor supported by two-lobe hydrodynamic journal bearings operating with a non-Newtonian lubricant. Proceedings of the Institution of Mechanical Engineers, Part J: Journal of Engineering Tribology, 233(6), 884–898.